



# Evolution of the Heliotail Lobes over a Solar Cycle as Measured by IBEX

M. A. Dayeh<sup>1,2</sup>, E. J. Zirnstein<sup>3</sup>, S. A. Fuselier<sup>1,2</sup>, H. O. Funsten<sup>4</sup>, and D. J. McComas<sup>3</sup>

<sup>1</sup>Southwest Research Institute, San Antonio, TX 78238, USA; [maldayah@swri.edu](mailto:maldayah@swri.edu)

<sup>2</sup>University of Texas at San Antonio, San Antonio, TX 78249, USA

<sup>3</sup>Department of Astrophysical Sciences, Princeton University, Princeton, NJ 08544, USA

<sup>4</sup>Los Alamos National Laboratory, Los Alamos, NM 87545, USA

Received 2022 February 18; revised 2022 April 27; accepted 2022 May 17; published 2022 July 27

## Abstract

Energetic neutral atom (ENA) measurements by IBEX reveal that the heliotail comprises an energy-dependent multilobe structure. We examine the heliotail evolution over 11 yr of IBEX observations covering a full solar cycle (SC). We find the following: (1) The heliotail structure persists over the entire SC, comprising three ENA-enhanced and two ENA-suppressed lobes. (2) Lobe sizes and locations are generally stable but exhibit variations in ENA fluxes driven by the SC. (3) Lobe centers follow a cyclic behavior over multiple SC phases, indicating direct signatures of slow and fast solar wind (SW) interactions in the inner heliosheath (IHS). (4) The tilted plane passing through the port–starboard lobes’ centers oscillates in latitude but maintains its tilt from the ecliptic plane, likely a consequence of the interstellar magnetic field draping around the heliosphere. (5) The transition of the central heliotail from a single lobe at  $\sim 1.1$  keV to two lobes above  $\sim 2$  keV is SC-dependent and directly reflects the IHS plasma properties, i.e., when ENA fluxes from fast SW from the polar coronal holes change over time. (6) The central lobe exhibits a substructure that is enhanced and offset from the downwind direction, possibly indicating an asymmetric ENA emission or an asymmetry in the parent plasma distribution. These results reveal the general stability of the heliotail structure over time and distinct variations in individual lobes’ properties in relation to the SC phases. Furthermore, results show the effects of multiple SC phases in the tail, reflecting different ENA travel times and source histories.

*Unified Astronomy Thesaurus concepts:* [Heliosphere \(711\)](#); [The Sun \(1693\)](#); [Charge exchange ionization \(2056\)](#); [Solar cycle \(1487\)](#); [Interstellar medium \(847\)](#); [Solar wind \(1534\)](#)

## 1. Introduction

The solar wind (SW) plasma flows out continuously and radially from the Sun at supersonic speeds. Interstellar neutrals, mostly hydrogen atoms, drifting through the heliosphere unaffected by magnetic and electric fields, ionize through charge exchange or photoionization, creating pickup ions (PUIs) that interact with the SW plasma. The PUIs are then carried outward with the SW flow. This SW and PUI population eventually slows down to subsonic speeds at the heliospheric termination shock (HTS). Beyond the HTS, the shocked (slowed and heated) SW and preferentially accelerated PUIs populate the inner heliosheath (IHS) region, bounded by the HTS and a tangential discontinuity that separates it from the local interstellar medium (LISM) plasma, known as the heliopause. The location of the heliopause is determined by pressure balance between the magnetized plasma on both sides, with latitudinal and temporal variations in the SW dynamic pressure, and the symmetrizing effect of charge exchange with interstellar neutrals (e.g., Pogorelov et al. 2009). Further charge exchange between the IHS plasma and interstellar neutrals creates energetic neutral atoms (ENAs) that travel across large distances, carrying inherent properties of their source regions (e.g., Baranov & Malama 1993; Fahr et al. 2000; Alexashov & Izmodenov 2005; Pogorelov et al. 2006; Izmodenov et al. 2009; Opher et al. 2009; Heerikhuisen et al. 2010; Zirnstein et al. 2014, 2021; Zank 2015). ENAs thus provide the unique

capability of probing physical processes and interactions from distant plasma regions and boundaries of the heliosphere.

The Interstellar Boundary Explorer (IBEX; McComas et al. 2009a) is an Earth-orbiting spacecraft that utilizes two single-pixel cameras (Funsten et al. 2009a; Fuselier et al. 2009b) to provide global observations of ENAs of heliospheric origin for the first time (e.g., McComas et al. 2009b; Schwadron et al. 2009b). Launched in 2008, IBEX measurements have already covered a full solar cycle and continue to provide crucial observations and pioneering knowledge about the SW–LISM interaction (McComas et al. 2020). Among the prime discoveries are the presence of the IBEX ribbon (Funsten et al. 2009b; Fuselier et al. 2009a; McComas et al. 2009b, 2014; Schwadron et al. 2009a) and the properties of the pristine LISM (e.g., Möbius et al. 2009, 2012, 2015; Bzowski et al. 2012, 2015; McComas et al. 2012a, 2015; Schwadron et al. 2013, 2015; Kubiak et al. 2016; Zirnstein et al. 2016b). IBEX measurements have also provided a plethora of new information about the IHS dominant physical mechanisms and properties (e.g., Schwadron et al. 2011, 2014; Dayeh et al. 2012; McComas et al. 2012c, 2013, 2014; Zirnstein et al. 2016a), as well as observational evidence of a distinctly structured heliotail (e.g., McComas et al. 2013; Zirnstein et al. 2017b).

The shape of the heliotail is a fundamental heliospheric unknown and a subject of active research within the community. McComas et al. (2013) provided the first-ever analysis of the heliotail using the first 3 yr of IBEX observations. These authors showed that the heliotail exhibits a multilobe structure created by slow and fast SW at low and high latitudes, respectively. They also showed that the



Original content from this work may be used under the terms of the [Creative Commons Attribution 4.0 licence](#). Any further distribution of this work must maintain attribution to the author(s) and the title of the work, journal citation and DOI.

low-latitude portion is tilted by  $\sim 10^\circ$  with respect to the ecliptic plane, an observation that was interpreted as a consequence of the interstellar magnetic field (ISMF) tension force that squeezes the heliopause and rotates it toward its direction in space. Zirnstein et al. (2016a) further showed that in addition to this tilt, the northern lobe and southern lobe lie on a plane that is nearly perpendicular to the solar equatorial plane indicating a strong relation between heliotail ENAs and the heliolatitudinal structure of the SW originating from the Sun. McComas et al. (2013) further suggested that the observed heliotail structure demonstrates the intermediate nature of the heliosphere's interstellar interaction, where both external dynamic and magnetic pressures strongly affect the heliosphere (McComas et al. 2009b, after Parker 1961).

Schwadron et al. (2014) separated the ribbon from the globally distributed fluxes and found that the heliotail is offset from the downwind direction by  $\sim 10^\circ$ , interpreting this as a result of the asymmetric pressure that the ISMF puts on the heliosphere. Using the ENA maps acquired during the first 5 yr of IBEX with the ENA ribbon excluded (separated data from Schwadron et al. 2014), Zirnstein et al. (2016a) performed a detailed analysis of the heliotail, quantifying the geometry of five lobes: a central lobe (C-lobe) at  $\sim 1.1$  keV, and a portside lobe (P-lobe), a starboard lobe (SB-lobe), a northern (N-lobe), and a southern lobe (S-lobe) at energies above  $\sim 2$  keV. These authors quantified the center locations of these lobes, and found that the heliotail lobes at  $> 2$  keV have a strong correlation with the asymmetric structure of the IHS flow around the Sun. In particular, the P-lobe and SB-lobe formation is driven by the asymmetric heliosheath flows, a large nose-tail asymmetry of the distance to the HTS and thus of the relative PUI density at the HTS, and by the energy-dependent removal of PUIs via charge exchange in the IHS. In a separate study, Zirnstein et al. (2020) further derived the distance from the Sun to the source of  $\sim 1$ – $6$  keV ENAs in the heliotail as a function of time exceeding  $\sim 300$  au, concluding that the ENA source distances seen by IBEX are related to the plasma properties being observed. For instance, the consistent increase in ENA source distance in the time period 2009–2013 to 2014–2017 as derived by Zirnstein et al. (2020) suggests that IBEX observes a fast/hotter plasma parcel propagating down the heliotail before being replaced by slow/cooler plasma as the solar cycle evolves.

Numerical simulations of the heliosphere's shape and its dominant processes provide crucial information on the heliotail. Recent developments in simulations have caused disagreement in our understanding of the shape of the heliotail. Using a coupled MHD-neutral hydrogen plasma simulation and assuming a unipolar solar magnetic field and steady-state boundary conditions, Opher et al. (2015) suggested that the heliotail splits into a croissant-like shape, where SW plasma is largely confined and collimated northward and southward of the equatorial plane, of a relatively short tail (a few hundred astronomical units). Using the same boundary conditions of Opher et al. (2015), simulations by Pogorelov et al. (2015) did show collimation of the flow at high latitudes; however, they did not reproduce a short, croissant-like tail but rather a very elongated tail. These authors further showed that the kinetic treatment of neutrals and the 11 yr solar cycle both counteract the SW collimation created by the croissant-like structure. Pogorelov (2016) and Zhang & Pogorelov (2016) also argued that the heliotail must be a very long structure in order to

properly explain TeV cosmic rays measured at 1 au (e.g., Abbasi et al. 2012; Schwadron et al. 2014). The results of Izmodenov & Alexashov's (2015, 2020) modeling of the heliosphere also showed that the unipolar magnetic field assumption drives the two-lobe SW collimation process reported by Opher et al. (2015), but does not produce a croissant-like heliosphere, potentially due to either the effects of charge exchange or the numerical fitting of the heliopause. The effects of charge exchange reported by Pogorelov et al. (2015) and Izmodenov & Alexashov (2015) appear to be contradictory to those recently reported by Opher et al. (2021), who suggest that instabilities driven by the introduction of charge exchange in the heliosphere model drive the development of the two-lobe heliotail structure.

Zirnstein et al. (2017b) performed a time-dependent heliosphere simulation that included slow and fast SW variations over a solar cycle and produced a comet-like heliotail, further showing that the solar cycle drives the heliotail lobes with properties very similar to those observed by IBEX. The authors showed that the shapes and locations of the heliotail ENA lobes are reproduced by PUIs that are preferentially heated at the HTS, and are directly influenced by the PUI temperatures in the slow versus fast SW. Finally, recent simulations by Kornbleuth et al. (2020, 2021) and Baliukin et al. (2020) using different ENA models with different kinetic-MHD plasma solutions and boundary conditions were also able to qualitatively reproduce a heliotail profile similar to the one observed by IBEX, although their numerical solutions for the distant heliotail were significantly different—one producing a croissant-like heliotail and the other a comet-like tail. Thus, it seems clear that the discrepancy of the heliosphere's shape between different models is partially owed to the different methods of numerical solution. Observation-based analyses of the heliotail structure using IBEX observations can provide crucial constraints that may help discriminate between the proposed structures of the heliotail.

In this paper, we provide a detailed analysis of the heliotail structure and its temporal and spatial variations using 11 yr of IBEX data, thus covering a full solar cycle. We particularly show that the heliotail lobes are persistent structures, but exhibit distinct trends that are likely driven by solar cycle variations.

## 2. Data

We use the validated sky maps from the IBEX-Hi instrument at  $6^\circ$  resolution. The data is produced by the IBEX Science Operations Center, which periodically validates and provides products to the official IBEX data release website.<sup>5</sup> The product used here is from Data Release #16, for which the citable reference, documentation, and validation is McComas et al. (2020). For this analysis, we use the annually combined, ENA sky maps spanning 11 yr between 2009 January and 2019 December at five different energy passbands, centered at  $\sim 0.7$ ,  $\sim 1.1$ ,  $\sim 1.7$ ,  $\sim 2.7$ , and  $\sim 4.3$  keV. The annual sky maps are in the ram direction and in the spacecraft frame; the data incorporates survival probability correction, which corrects for losses of ENAs by ionization from  $\sim 100$  to 1 au. The maps are plotted in ecliptic J2000 coordinates and centered on the downwind direction ( $75^\circ.7$ ,  $-5^\circ.1$ ; McComas et al. 2015). In all maps shown, the port side is on the right side of the map.

<sup>5</sup> <https://ibex.princeton.edu/DataRelease>

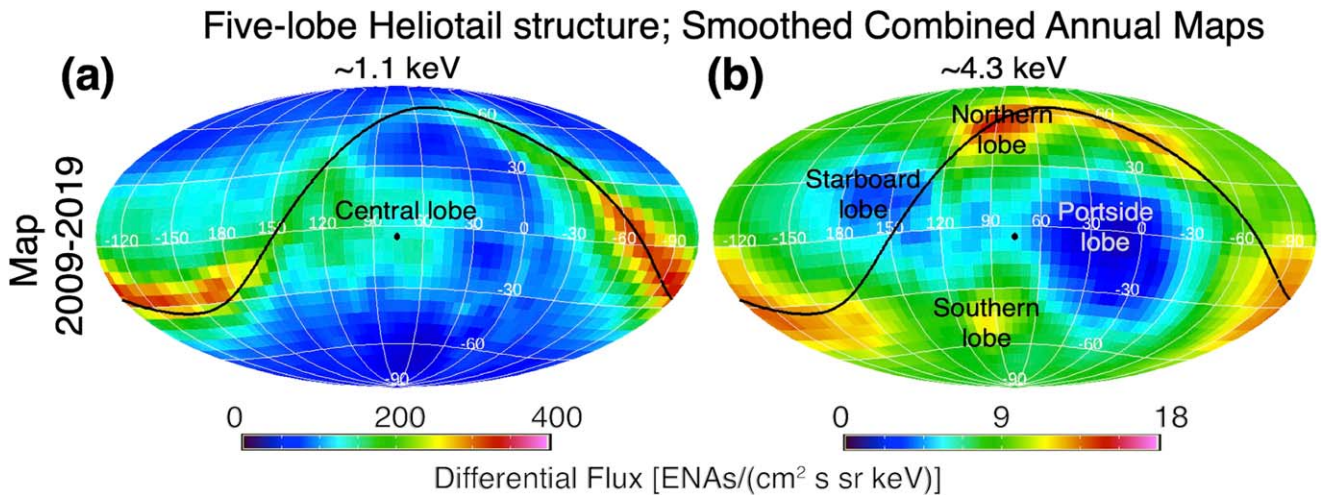


**Figure 1.** Structure of the five-lobed heliotail as it appears at  $\sim 1.1$  and  $\sim 4.3$  keV in the 11 yr (2009–2019) combined smoothed maps. The black trace corresponds to the ribbon location in the sky. The characteristic heliotail lobes are indicated: (a) central ENA enhancement at  $\sim 1.1$  keV and (b) northern and southern ENA enhancements, in addition to port and starboard ENA depressions. The black line here indicates the energy-averaged ribbon path (Dayeh et al. 2019).

### 3. Observations

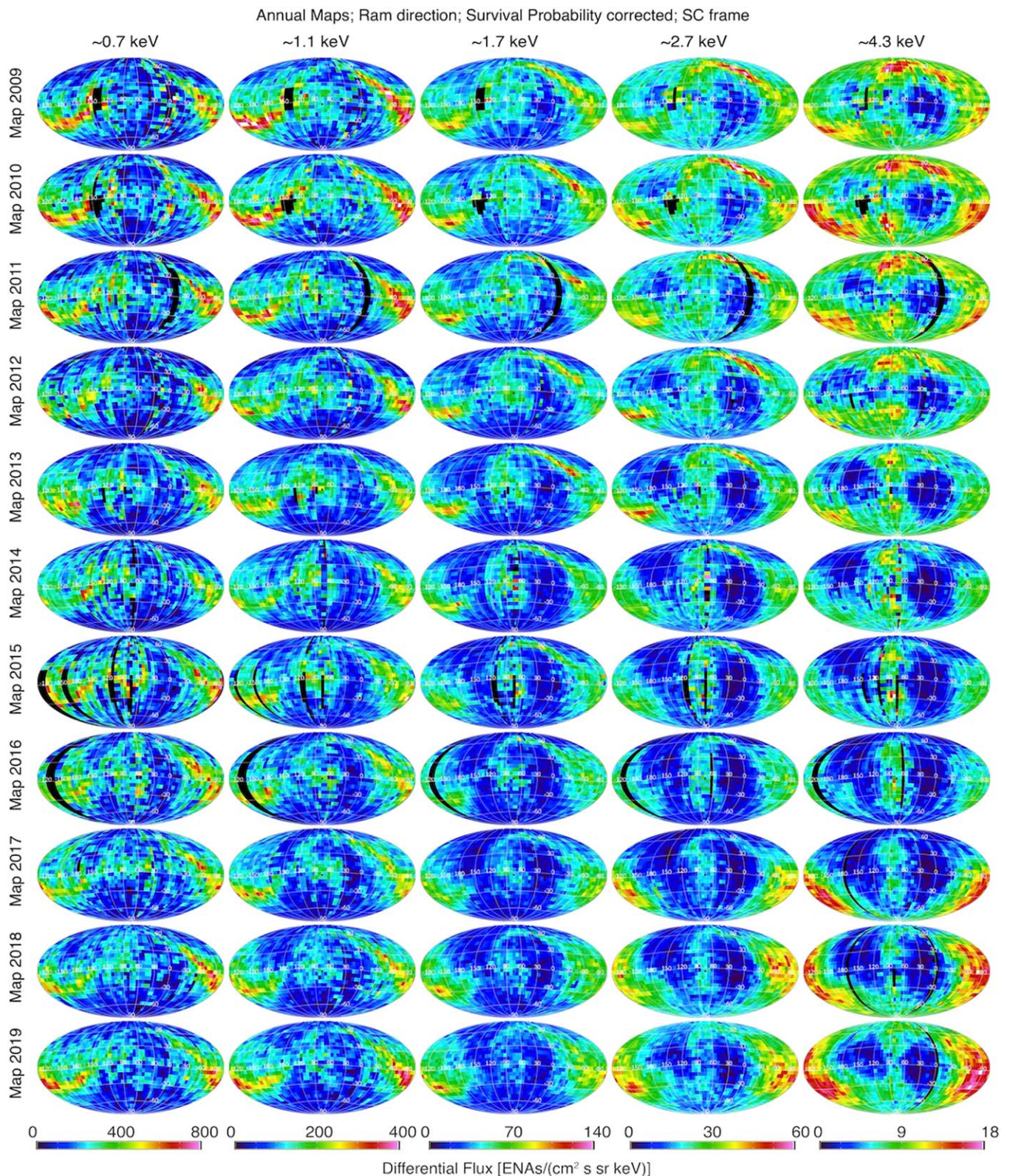
#### 3.1. The Structure of the Heliotail over a Solar Cycle

Figure 1 shows an IBEX heliospheric ENA sky map centered in the downwind direction, showing the structure of the heliotail, as first reported by McComas et al. (2013) and later substantiated by Zirnstein et al. (2016a). The characteristic five lobes of the heliotail stand out; one of these is (i) the ENA-enhanced C-lobe at  $\sim 1.1$  keV, which appears as a blob around the downwind direction (Figure 1(a)). Notice that the ribbon passes close to it. There are also the four labeled lobes at  $> 2$  keV, most prominent at the highest energy of  $\sim 4.3$  keV: (ii) the ENA-suppressed P-lobe and SB-lobe (appearing in dark blue) and (iv), (v) the ENA-enhanced N-lobe and S-lobe. The black line marks the best-fit circle to the averaged ribbon centered on ( $\text{lon} = 218^\circ 33$ ,  $\text{lat} = 40^\circ 38$ ;  $\text{radius} = 74^\circ 81$ ) over all energies, as determined by Dayeh et al. (2019). This figure serves as a guide to the tail lobes and their position in the sky for all map plots in the paper.

Figure 2 shows the downwind-centered annual sky maps obtained by IBEX-Hi during 2009–2019 (columns) and for five IBEX-Hi energy passbands (rows). The same color scale is shown for each energy passband across all years for easy comparison among the maps. It is important to note that the ribbon has not been separated from this data, in contrast to previous studies (e.g., Schwadron et al. 2014; Zirnstein et al. 2016a), and thus in all maps, the ribbon appears across the sky, most prominently at northern latitudes, and passes in the starboard side, most apparent at  $\sim 1.1$  keV. The ribbon here heavily contaminates the N-lobe in some years. The latter is most pronounced at  $\sim 4.3$  keV, where its flux is clearly higher than that of the ribbon at this energy (the ribbon is brightest at  $\sim 1.1$  keV). The time evolution of the sky maps in Figure 2 clearly shows two main changes: (1) temporal variations at each energy step, with those at  $\sim 4.3$  keV being the most pronounced (last column) and (2) variation between energies (e.g., last row). The former indicates that the downwind direction, which includes the heliotail region, undergoes variations as a function of time. Note that these maps show the downwind (center) and upwind (edges) extent of the sky. The maps start at relatively high fluxes for the first 3 yr between 2009 and 2011, during solar minimum conditions

when the SW has significant latitudinal asymmetry and the high latitudes are well lit up with ENAs. Then, it dims between 2012 and 2016 (solar maximum) and brightens back in 2017 onward, nearly to its original ENA levels during the first 3 yr. This is a periodic effect that is indicative of the solar cycle. In interpreting these maps, it is important to keep in mind that there is a large difference between upwind and downwind ENA return times, and that ENA brightness changes are shifted from the nominal SW solar cycle observation times by several years, depending on the ENA energy and distance to the ENA source. For instance, in the upwind direction, it takes about  $\sim 2$ – $3$  yr for the SW with speed  $\sim 500$  km s $^{-1}$  to travel from the Sun to the center of the IHS, charge-exchange with ENAs, and come back to 1 au, assuming the HTS is at  $\sim 90$  au. In the downwind direction the case is different. For an HTS distance of 160 au (McComas et al. 2019), the SW would travel for  $\sim 1.5$  yr to the HTS (assuming a 500 km s $^{-1}$  speed). If the flow speed is  $\sim 150$  km s $^{-1}$  downstream, and the cooling distance in the downwind direction is 129–329 au (Zirnstein et al. 2020 using IBEX observations for two time periods), that would result in a plasma flow time of 4–10 yr. Adding the ENA travel time back to Earth brings the total travel time to  $> 7$  yr.

To further improve the counting statistics, we statistically combine the annual sky maps into five different time periods from 2009 to 2019, as shown in Figure 3(a). The combinations largely help in enhancing ENA statistics by reducing flux uncertainties between neighboring pixels. On average, the combined maps have qualitatively comparable fluxes at each of the energy passbands and thus the solar cycle trend is maintained. Similar averaging has been used previously for analysis purposes (e.g., Zirnstein et al. 2017a; Dayeh et al. 2019; Schwadron & McComas 2019; McComas et al. 2020). The first set of combined maps includes years 2009–2011, when ENA fluxes were the brightest; the second set includes the following two sky maps 2012–2013, the third set 2014–2015, and the fourth set 2016–2017; and finally the fifth set includes 2018–2019, when the ENA fluxes were enhanced again. In order to do a global analysis on the downwind direction and a sequential comparison of large features in the sky, pixel-to-pixel fluctuations ought to be suppressed in a consistent way. One way to do this is via statistical smoothing, which has been used and validated



**Figure 2.** Mollweide projections of IBEX-Hi annual (ram-direction) ENA sky maps, centered on the downwind direction. Columns represent the five different energy passbands and rows show maps of the 11 sequential years from 2009 to 2019. Black swaths are regions with no data.

successfully in similar analyses and interpretations of IBEX heliospheric (e.g., McComas et al. 2013; Zirnstein et al. 2017a) and magnetospheric (McComas et al. 2012b) observations. The importance of smoothing for global analysis is that it suppresses pixel-to-pixel fluctuations but

keeps larger-scale, global structures and their temporal variations intact. This in turn enables a more consistent examination of the spatial and temporal evolution of these structures. Figure 3(b) shows the smoothed maps. Here, we use a  $9^\circ$  smoothing angular window (solid angle) across the

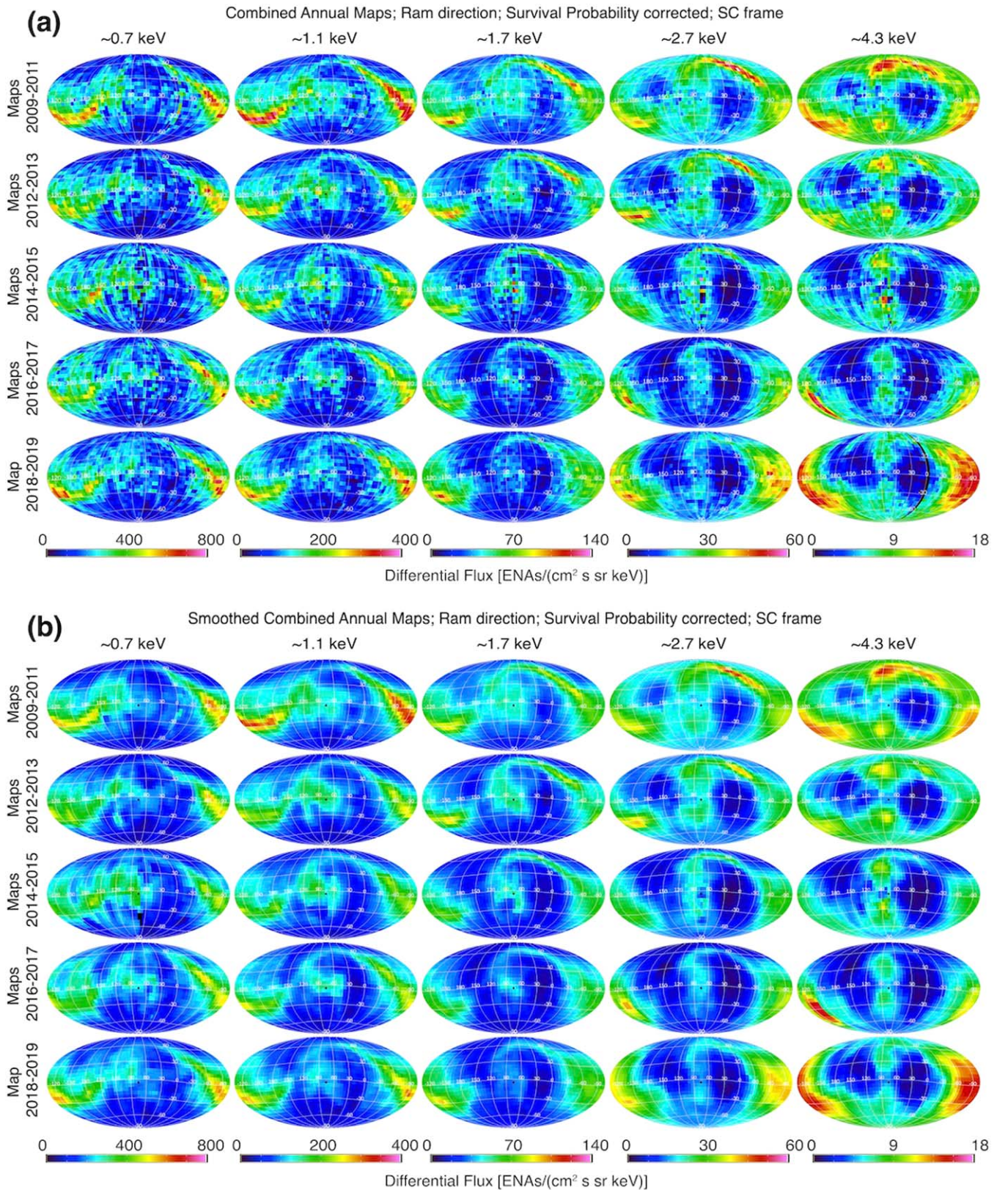


**Figure 3.** (a) Combined IBEX-Hi ENA maps over five periods, as follows: [2009–2011], [2012–2013], [2014–2015], [2016–2017], and [2018–2019]. The layout is similar to that of Figure 2. (b) Statistically smoothed maps of Figure 3(a). A smoothing window of  $9^\circ$  is applied (see text for details).

sky. Each pixel's flux value is replaced by the weighted mean flux of the surrounding pixels within this window, along with the associated combined statistical and propagated uncertainties. For a given set of pixels with flux  $\{j_i \pm \sigma_i\}_{i=1}^n$ , the

weighted mean value is

$$\mu_{\text{weighted}} = \frac{\sum_{i=1}^n j_i / \sigma_i^2}{\sum_{i=1}^n 1 / \sigma_i^2} \quad (1)$$

and the associated total uncertainty is the combination of the propagated and statistical uncertainties,

$$\sigma_{\text{total}} = \sqrt{(\sigma_{\text{mean}}^{\text{prop}})^2 + (\sigma_{\text{mean}}^{\text{stat}})^2} \quad (2)$$

where

$$\sigma_{\text{mean}}^{\text{prop}} = \frac{1}{\sqrt{\sum_{i=1}^n 1/\sigma_i^2}} \quad (3)$$

and

$$\sigma_{\text{mean}}^{\text{stat}} = \sqrt{\frac{\frac{1}{n}(\sum_{i=1}^n 1/\sigma_i^2)^2}{(\sum_{i=1}^n 1/\sigma_i^2)^2 - \sum_{i=1}^n 1/\sigma_i^4} \frac{\sum_{i=1}^n (j_i - j_{\text{mean}})^2/\sigma_i^2}{\sum_{i=1}^n 1/\sigma_i^2}}. \quad (4)$$

Note that Equation (3) is the propagation of uncertainties of the sampling values and Equation (4) is caused by the variability of the sampled values. For different applications of these statistics, see Zirnstein et al. (2016b), Livadiotis (2018), and Dayeh et al. (2019, 2020a, 2021).

Conditions of  $j_i \geq \sigma_i$  and at least three nonzero pixels are required in the surroundings of a particular pixel in order for it to be smoothed. The solid-angle window accounts for projection effects so that at higher latitudes, the smoothing window covers more pixels. Comparing Figures 3(a) and (b), we note that the global structures are maintained, but the maps are now smooth enough for us to identify boundaries between the different apparent structures.

### 3.2. Isolating the Heliotail Lobes

In order to examine the evolution of the heliotail lobes (Figure 1), we devise a method to isolate the lobes in a consistent manner at energies  $\sim 1.1$  and  $\sim 4.3$  keV. We do this by first setting a  $40^\circ$  (ENA-enhanced lobes) to  $70^\circ$  (ENA depression lobes) angular window around each lobe; the lobe centers used here are from Zirnstein et al. (2016a), except for the C-lobe, for which we use the downwind direction as a starting point. We then mask around the particular lobe of interest and calculate the averaged flux within the isolated region. The lobe boundaries are then determined by calculating isosurface contours at percentages above or below the derived averaged flux, namely,  $>30\%$  for the enhanced C-, N-, and S-lobe and  $<30\%$  for the suppressed P- and SB-lobe. Varying these thresholds would vary the contoured lobe boundaries; therefore, we perform a sensitivity analysis in which we vary the thresholds by 10% up and down from the nominal threshold and derive the averaged contour. However, we emphasize that using a consistent threshold across all maps is important to properly examining the spatial and temporal evolution of the lobes. The threshold value of 30% is chosen because it provides the greatest number of bounded lobes for all time periods. Figure 4 shows a demonstration of the lobe isolation method on the P-lobe of the smoothed map obtained for 2009–2011. Figure 4(a) shows the  $70^\circ$  masked region around the P-lobe. Figure 4(b) shows the inferred isolated P-lobe; the red contour marks the derived boundary of the P-lobe, which includes fluxes that are 30% below the averaged ENA value determined from Figure 4(a). White and yellow traces indicate the boundaries after the 30% threshold is varied up and down by 10%. As shown, the boundaries vary slightly; we have tested this for all lobes and determined that varying the

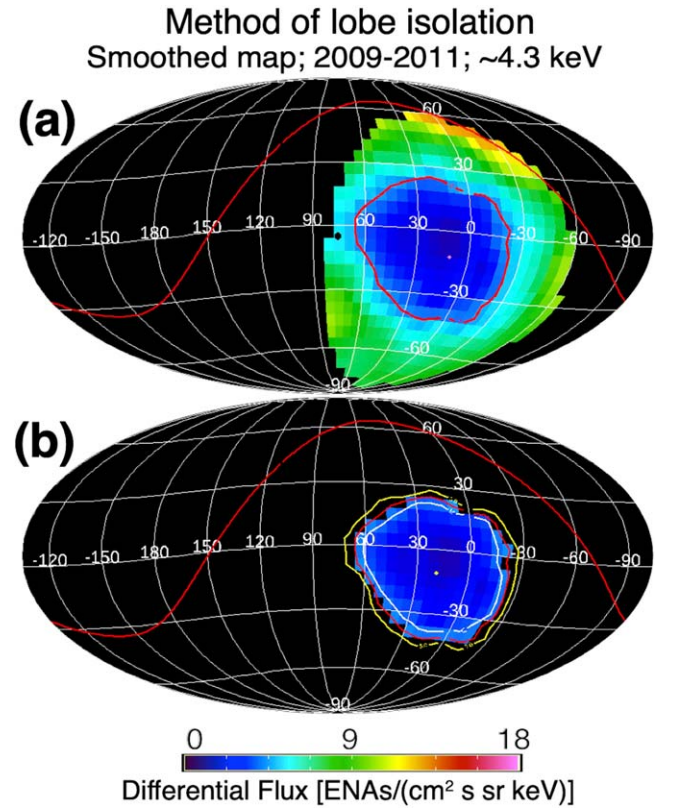


**Figure 4.** Demonstration of how lobe boundaries are determined. (a) A large solid angle is drawn around the lobe of interest and the weighted-average flux is determined. (b) A threshold below (this case) or above the averaged flux constrains the lobe contour. The three contours shown mark the 10% variability around the threshold value. See text for details.

thresholds does not significantly affect the overall analysis results and conclusions. We thus emphasize that while this method of isolating the lobes is a heuristic approach, using it in a consistent manner for all lobes enables useful analysis and subsequent interpretation of the heliotail lobes.

Once the contours are determined for each lobe at the three thresholds, we determine the averaged contour and next calculate a new lobe center that is weighted by the fluxes (akin to a center of mass). This is done by converting each pixel location to a single unit vector weighted by its flux, summing all locations and normalizing the resulting vector. We also calculate the area of each resulting lobe by summing over all individual pixels and properly accounting for the map projection effect. Finally, we calculate the weighted-average ENA flux of each isolated lobe. Note that all weighted-average values and their associated uncertainties (Equations (1) and (2)) are determined and properly propagated throughout the different layers of the analysis. Also note that the 10% threshold adjustment in the determination of each lobe is incorporated in the quantification of variability in lobe properties (flux, center, and area).

We remark that some lobes during some periods fail to be confined using the described contouring method, either because the fluxes do not match the contouring criteria (e.g., S-lobe in 2018–2019), or when the lobes are heavily contaminated by the ribbon (e.g., N-lobe in 2009–2011 and 2018–2019). For these cases, no data are reported. Table 1 shows a summary of the derived lobe properties for different energies and time periods, along with the overall averages.

**Table 1**  
Derived Properties of All Lobes

		ESA 3 ( $\sim 1.1$ keV)		ESA 6 ( $\sim 4.3$ keV)							
		C-lobe		N-lobe		S-lobe		P-lobe		SB-lobe	
		$\mu_{\text{weighted}}$	$\sigma_{\text{total}}$								
2009–2011	$J_{\text{ENA}}$	140.36	4.38	...	...	10.67	0.38	2.88	0.17	4.65	0.30
	A	2396.43	607.99	...	...	320.03	148.01	4310.95	523.27	2576.95	1167.35
	$C_{\text{lon}}$	95.93	5.05	...	...	95.56	1.58	18.10	0.20	147.29	1.51
	$C_{\text{lat}}$	1.78	0.29	...	...	-46.14	0.19	-10.57	1.00	12.99	2.45
2012–2013	$J_{\text{ENA}}$	146.83	3.83	9.98	0.35	9.64	0.45	2.05	0.09	3.19	0.21
	A	2988.76	298.26	1223.40	229.97	553.18	198.97	4459.17	368.29	3377.50	986.47
	$C_{\text{lon}}$	89.59	0.48	86.64	1.78	84.93	2.61	8.56	0.61	161.25	1.39
	$C_{\text{lat}}$	2.83	0.56	47.45	0.99	-35.09	1.75	-9.76	0.79	16.34	0.40
2014–2015	$J_{\text{ENA}}$	146.92	3.03	7.12	0.43	7.52	0.34	1.39	0.08	1.94	0.10
	A	2843.71	294.65	2120.58	268.34	1062.41	236.14	4017.89	512.29	1886.33	393.52
	$C_{\text{lon}}$	90.39	1.52	89.28	1.30	88.00	0.67	11.10	1.12	178.01	1.76
	$C_{\text{lat}}$	3.80	0.54	38.51	1.67	-37.53	1.85	-6.29	1.85	36.87	1.82
2016–2017	$J_{\text{ENA}}$	129.27	2.69	5.21	0.14	5.99	0.24	1.44	0.08	1.54	0.11
	A	2070.57	270.57	2937.26	161.63	1184.15	139.12	3273.05	495.1	1354.86	404.55
	$C_{\text{lon}}$	79.00	0.28	83.36	0.24	83.44	0.32	9.43	0.17	162.73	0.89
	$C_{\text{lat}}$	4.77	0.35	36.05	0.89	-28.94	1.48	3.20	0.11	52.9	2.31
2018–2019	$J_{\text{ENA}}$	111.93	3.34	...	...	...	...	1.94	0.12	2.24	0.14
	A	1694.05	642.39	...	...	...	...	4835.53	455.95	3704.81	670.86
	$C_{\text{lon}}$	89.77	2.13	...	...	...	...	25.25	0.37	145.18	1.43
	$C_{\text{lat}}$	6.87	0.25	...	...	...	...	0.26	0.14	17.89	1.02
2009–2019	$J_{\text{ENA}}$	133.95	6.80	5.98	1.57	7.68	1.14	1.71	0.21	2.10	0.37
	A	2532.59	278.09	2321.74	556.44	774.44	243.42	4237.85	328.01	2057.46	507.60
		$\mu_{\text{unweighted}}$	$\delta_{\text{unweighted}}$								
2009–2019	$C_{\text{lon}}$	88.94	6.14	86.43	2.97	87.98	5.39	14.49	7.09	158.89	13.31
	$C_{\text{lat}}$	4.01	1.95	40.67	6.00	-36.93	7.13	-4.63	6.11	27.41	17.05

**Note.**  $C_{\text{lon}}$ ,  $C_{\text{lat}}$ , A, and  $J_{\text{ENA}}$  indicate the weighted quantities of the lobe center longitude [deg], lobe center latitude [deg], lobe area [deg<sup>2</sup>], and ENA averaged flux. The symbols  $\mu$  and  $\sigma_{\text{total}}$  indicate the mean value and the total uncertainty, which combines both the propagated and statistical uncertainties. Nonweighted averages of all centers are also provided in the last two rows along with their corresponding standard deviation ( $\delta_{\text{unweighted}}$ ) values. Empty cells correspond to times when lobe boundaries could not be resolved using the used criteria.

### 3.3. Variation of the Heliotail Lobes

Figure 5 shows the derived contours for all five lobes superposed on the sky grid and color coded to highlight the evolution over the five time periods. The contours shown are the averages over the three threshold levels used in deriving the ribbon boundaries (10% above and below), and the centers

are the weighted-average centers. The ribbon central trace is marked by the black line. Figure 5(a) shows the evolution of the P-lobe of the heliotail. The lobe contouring converges to a bounded value for all time periods, with lobe centers varying within  $\sim 30^\circ$  from each other in longitude and latitude. The average center of all times for this lobe is close to the ecliptic

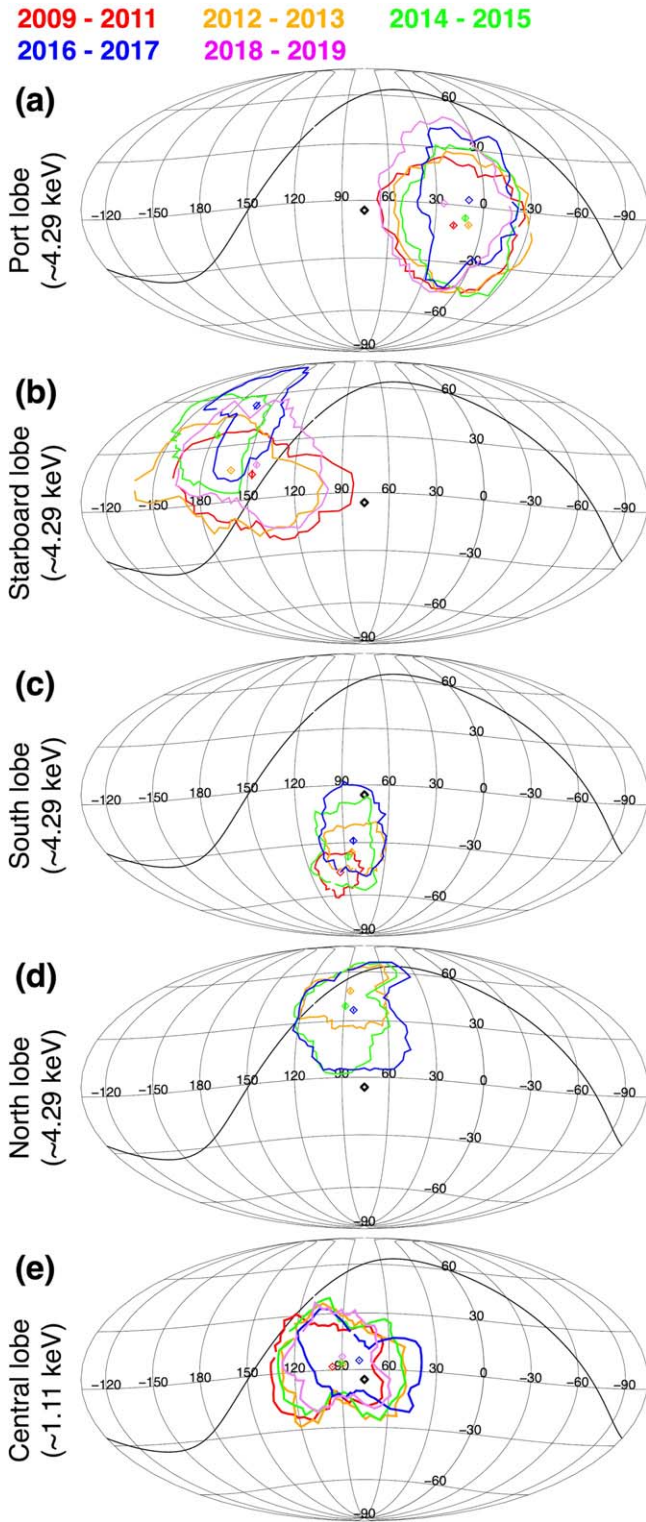


**Figure 5.** Lobe contours on a Mollweide projection during the five studied time periods, color coded by time. Each contour represents the average boundaries with 10% variability around the flux threshold (see text for details). Missing contours for some periods indicate that the contour limit is too small or too large extending to the polar regions. The uncertainties of the contour regions are of the order shown in Figure 4.

plane [lon  $14^{\circ}49$ , lat  $-4^{\circ}63$ ; Table 1]. The contour traces show that the lobe extends northward during the last two periods but shrinks in longitude by roughly the same order ( $\sim 15^{\circ}$ ). Nonetheless, the lobe structure remains largely confined to

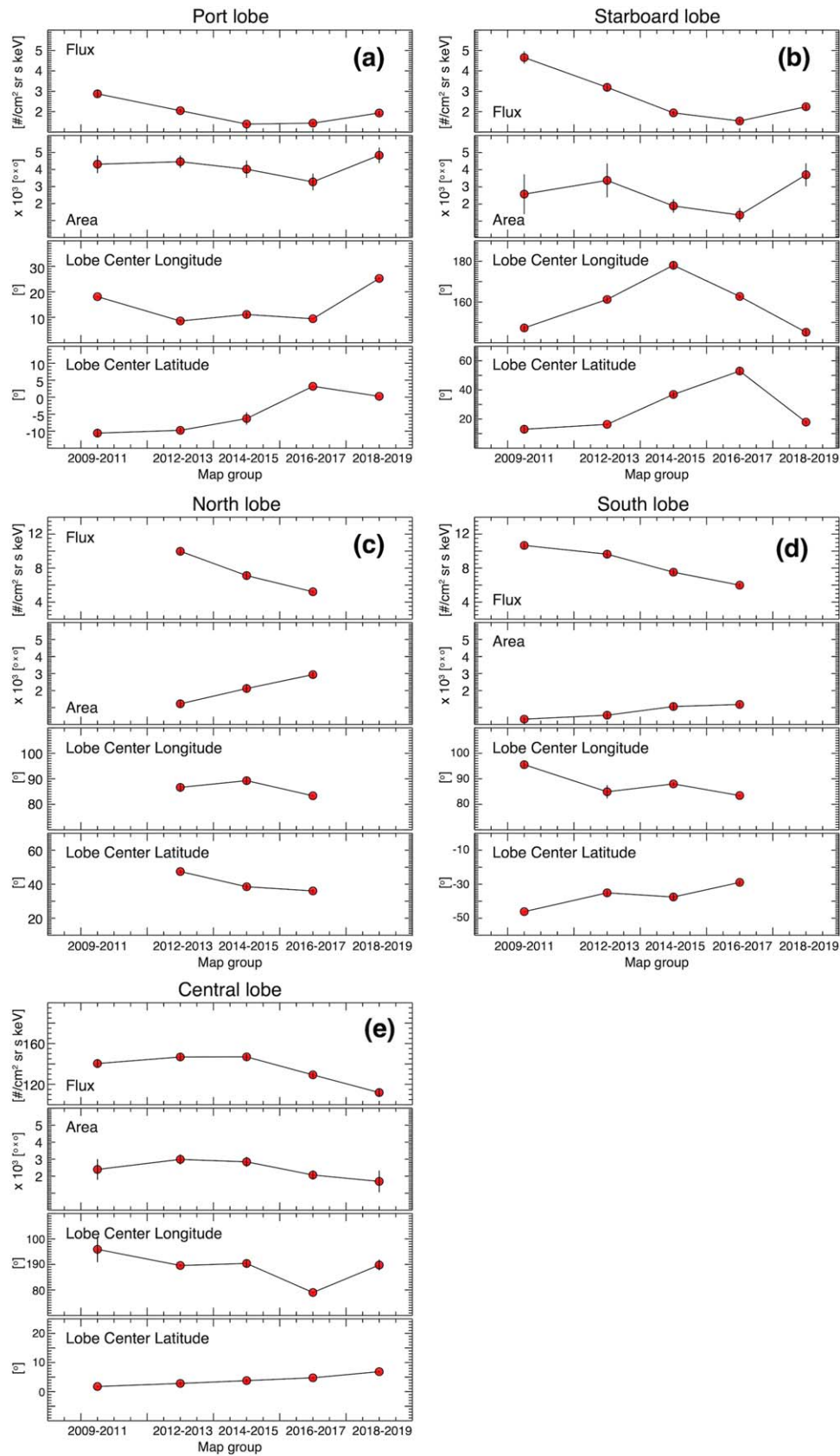
the same part of the sky. Averaged over all five periods, the P-lobe occupies the largest area among all lobes.

Figure 5(b) shows the SB-lobe contours. Here, the lobe isolation method also converges to a bounded contour during all periods. During 2014–2015 and 2016–2017, when ENAs in the sky dimmed, the SB-lobe shifted significantly to the northern latitudes. This lobe is also contaminated with the ribbon passing through it. The latter effect on the fluxes is not very significant since the  $\sim 1.1$  keV ribbon is faint at the higher energy of  $\sim 4.3$  keV. However, the ribbon’s passage creates an obstacle in the middle of this lobe, splitting it into two smaller lobes. This is the reason why this lobe appears elongated in longitude over a large area in the sky.

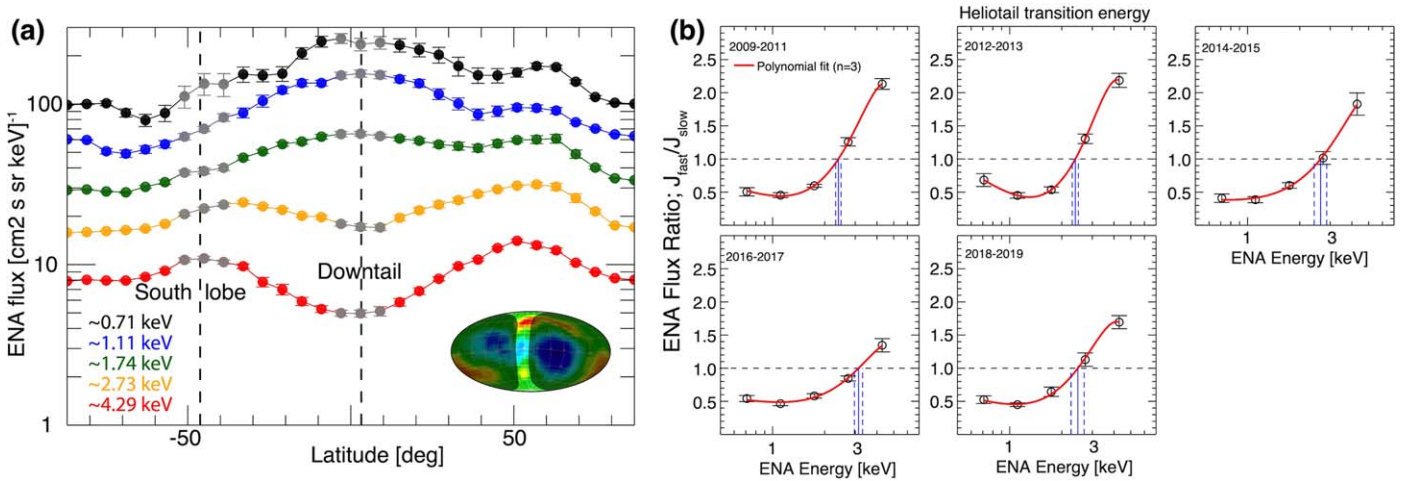
Figure 5(c) shows the heliotail S-lobe. This region is likely the cleanest in the sky since it is farthest from the ribbon. The lobe boundaries converge for four time periods and do not for 2018–2019. Although the lobe is clear in the ENA maps for this period (Figure 3(a)), it does not converge using the same contouring criteria applied to the other lobes because the lobe ENA enhancement does not exceed the threshold for providing a meaningful contour, and thus it is excluded. The four other lobe contours shown provide an interesting observation, where the lobes appear to increase in area as a function of time and simultaneously move northward toward the ecliptic. In contrast, the N-lobe, shown in Figure 5(d) for three time periods, behaves with an opposite moving trend, such that both lobes move toward the ecliptic as time progresses. This motion is discussed further in Section 4.

Figure 5(e) shows the geometry of the C-lobe as a function of time. The C-lobe is slightly offset from the downwind direction toward the starboard side, with the contour during 2009–2011 being the most offset from the downwind. The average location of the C-lobe for all time periods is  $88^{\circ}94$ , and thus the offset from the downwind direction is  $13^{\circ}24$ . A deviation from the downwind direction in the same direction and magnitude was also reported by Schwadron et al. (2014) and Zirnstein et al. (2016a) and interpreted as a possible result of asymmetry in the heliosphere. By looking at the ENA sky maps in Figure 3(a) and at the contours, one can easily spot that ENA fluxes in fact cover the full downwind region, but in an asymmetric way with the most enhanced ENA fluxes shifted toward the starboard direction. This is important as it indicates that ENA emissions do indeed come from an area surrounding the geometric downwind direction ( $180^{\circ}$  from the upwind/nose), but in an asymmetric way that creates this offset appearance. Finally, the rotational geometry of the C-lobe contours shows that the lobe is aligned with the direction of the port–starboard tilt reported elsewhere; such a tilt could be linked to other global processes such as the ISMF.

Figure 6 shows the variability of the lobes’ averaged flux, total area, and centers [longitude, latitude] as a function of time. Averages with corresponding uncertainties are determined using Equations (1) and (2). For the P-lobe shown in Figure 6(a), fluxes decrease over time and increase during the last period (2018–2019), but not to their initial flux levels during 2009–2011. The P-lobe area is generally fixed except for the period 2016–2017. One would expect that during solar maximum conditions, these ENA depressions would expand as the slow SW expands to higher latitudes, as is visible in Figure 3(b). The P-lobe center longitude moves south during years 2012 to 2017, and then moves back north to almost its initial location in 2009–2011, a cyclic motion that is likely



**Figure 6.** Variations of the heliotail lobes' properties over a solar cycle. Top to bottom in each plot: Variation of the mean ENA flux, area in the sky, and longitude and latitude of the respective weighted lobe center. Missing points indicate that the algorithm used does not converge to a meaningful value. As expected, the N-lobe has the least inferred information due to the ribbon's passage through it.



**Figure 7.** (a) Latitudinal variations of averaged ENA fluxes at all energies along an  $18^\circ$  swath in the downwind direction, highlighted in the inset map. Vertical lines indicate the downwind and S-lobe centers, representing the slow and fast SW regions, respectively. (b)  $R_J$  (Equation (5)) as a function of energy for all time periods. This illustrates the derivation of the heliotail transition energy as further discussed in the text.

indicative of the solar cycle effect. The latitude, however, appears to move northward for the first four periods and then slightly shifts course during the last period of 2018–2019. As a function of time, the SB-lobe, whose properties are shown in Figure 6(b), is also characterized by diminishing flux and an area that becomes smaller during 2014–2015 and 2016–2017, when the SB-lobe expands to higher latitudes. The center longitudinal motion clearly demonstrates the lobe’s motion northward during 2014–2015, then southward to its original location in 2009–2011. The motion of the center longitude of the SB-lobe behaves in an opposite way to that of the P-lobe. Figure 6(c) shows a dimming flux for the N-lobe, an area that increases with time, and a southward shifting location for the center of this lobe in terms of both latitude and longitude. For the S-lobe properties shown in Figure 6(d), fluxes also slightly dim with time, the area increases, and the lobe center shifts equatorward, similar to the N-lobe center motion. Finally, the evolution of the C-lobe properties in Figure 6(e) shows that ENA fluxes remain relatively constant during the first three periods and dim during the last two periods, the area is relatively fixed with a slight increase during 2012–2013 and 2014–2015, and the center varies over a narrow latitudinal region but a wider longitudinal region ( $\sim 20^\circ$ ). There is a sharp drop in the center longitude during 2016–2017 and the contouring method could contribute to this for this lobe, given the ribbon’s vicinity.

### 3.4. Apparent Splitting of the Heliotail

By tracking ENA sky maps as a function of increasing energy, e.g., Figure 2(b), it is apparent that the C-lobe at  $\sim 1.1$  keV elongates and eventually “splits” into the N- and S-lobe at higher energies, an observation that has also been discussed by other studies (e.g., Zirnstein et al. 2017b). These studies reproduced this energy-dependent structure using numerical simulations and found that this dependence happens because of the changing plasma properties in the IHS with increasing energy as a function of latitude. Using IBEX data, we revisit the heliotail structure using a data-based approach and estimate the energy at which the tail splits into two, northern and southern lobes.

Assuming that the splitting of the tail is strictly driven by the slow-to-fast SW transition as a function of latitude, the ratio of the high-latitude to the low-latitude ENA fluxes would enable us to close in on the energy at which the separation happens. This should be related to the ratio of the fast to the slow SW content. Figure 7(a) shows the latitudinal profile of the averaged ENA fluxes within  $18^\circ$  longitude around the downwind meridian during 2009–2011, as illustrated in the inset map (highlighted swath). Vertical dashed lines pass through the downwind center and the center of the S-lobe being studied ( $-46.14$  for this case). Both locations here are assumed to indicate ENA peaks coming from the slow SW and the fast SW, respectively. Using ENA fluxes at high latitude to represent the fast SW plasma distribution, and ENA fluxes at low latitude to represent the slow SW plasma distribution, we now calculate the ratio

$$R_J = \frac{J_{\text{fast}}}{J_{\text{slow}}} \quad (5)$$

where  $J_{\text{fast}}$  is the weighted-average flux along the selected S-lobe region and  $J_{\text{slow}}$  is the weighted-average flux along the selected downwind region, representative of the fast and slow SW transition as a function of latitude, respectively. Note that  $J_{\text{slow}}$  and  $J_{\text{fast}}$  vary over time in their respective S-lobe regions. For a nontransitioned heliotail (nonsplit),  $R_J$  is always below unity. Figure 7(b) shows these ratios for all energies and for each time period. In this figure, the horizontal line marks unity and the red curve is a third-order polynomial fit to all points. The blue vertical line shows the energy at which the ratio,  $R_J$ , equals 1. For the five periods, these values and their uncertainties are  $2.40 \pm 0.08$  keV for [2009–2011],  $2.40 \pm 0.10$  keV for [2012–2013],  $2.64 \pm 0.22$  keV for [2014–2015],  $3.13 \pm 0.17$  keV for [2016–2017], and  $2.48 \pm 0.21$  keV for [2018–2019]. The results show that the energy at which the tail transitions from a C-lobe to two lobes is not fixed over the years and rather varies by a significant factor. Nonetheless, the transitioning is persistent and does not disappear during any phase of the solar cycle.

#### 4. Discussion

We analyze the evolution of the heliotail structure over five multiyear periods using IBEX ENA observations spanning a full solar cycle. We find that (i) the heliotail five-lobe structure comprising the P-, SB-, N-, S-, and C-lobe is persistent in the sky for all time periods; (ii) the heliotail lobes exhibit specific temporal trends that are indicative of solar cycle phase effects; (iii) the energy at which the heliotail C-lobe ( $\sim 1.1$  keV) transitions into two lobes at higher energies ( $\sim 4.3$  keV) varies with the solar cycle phase, reflecting the closing and the opening of the polar coronal hole (PCH); (iv) the P-lobe and SB-lobe lie on a plane that is tilted with respect to the ecliptic plane; the tilting varies but is persistent across the entire 11 yr period; (v) ENA emissions from the C-lobe cover the entire downwind direction but exhibit an asymmetry that favors the starboard side; and (vi) the motions of the lobe centers indicate the presence of ENAs created from SW progenitors during different phases of the solar cycle. We further discuss these observations in the following sections.

##### 4.1. Origin of the Heliotail Lobes

Figure 8 schematically summarizes the main observations. For guidance, Figure 8(a) shows the evolution of the sunspot number between 2000 and 2020, with the solar minimum and maximum periods indicated. Figure 8(b) lists the estimated SW progenitor conditions of ENAs observed in the heliotail lobes based on ENA time delays determined from observations and simulations (Zirnstein et al. 2020, 2021). The estimated numbers are color coded to reflect their prospective creation times in different phases of solar cycles 23 and 24. Figure 8(c) shows the centers of all lobes and how they vary over the five time periods. Note that because the individual lobe centers are averages of contours from three threshold levels (the 10% variability explained earlier), their propagated total errors are asymmetric if the contours are asymmetric between the different thresholds (e.g., P1 and P4 in the S-lobe). The lobe centers are color coded to indicate their SW progenitor times in Figures 8(a) and (b). Superposed on the figure are indicators for the ecliptic, solar equatorial, and heliographic meridian planes (gray), along with the peak ribbon trace (violet), and the planes connecting the centers (nonweighted averages) of opposite-lobe pairs (red lines). Angles marking the relative locations of the lobes are also shown in the inset figure.

The locations and stability of the heliotail lobes' individual centers are visible in Figure 8(c), hovering within less than  $30^\circ$  of each other over an 11 yr period (except for the SB-lobe); the lobes' persistent presence indicates that they are a consequence of an inherent physical structure of the heliosphere, regardless of the solar cycle phase. To understand these trends, it is helpful to recall that all the lobes are created differently. The enhanced N-lobe and S-lobe are created by the fast SW input from the IHS at high latitudes during solar minimum, and by mixed slow and fast SW during solar maximum; the C-lobe is created by the slow SW populating the low latitudes input into the IHS. The P-lobe and SB-lobe are ENA depression lobes that are direct consequences of the IHS properties between the front/back and northern/southern regions of the heliosphere (Zirnstein et al. 2016a), almost disappearing during solar maximum conditions when the ENA global emissions at mid and low latitudes decrease. Here we recall that the SW and ENAs are delayed by a few to several years in different regions

of the heliotail, as indicated. The P-lobe and SB-lobe areas are thus created by emptying (i.e., when these ENA-lacking lobes expand, e.g., in years of SW maximum conditions) and filling (when they shrink due to ENAs populating more of the sky, e.g., in years of SW minimum conditions) in the surrounding areas of these lobes in the IHS. Since they are most pronounced at high energies, they are developed as the fast SW loading at higher latitudes increases (yielding smaller side lobes) or decreases (yielding larger side lobes). Zirnstein et al. (2016a) performed a comprehensive ENA modeling and were able to reproduce both lobe depressions by requiring a heliosheath thickness that expands with angle toward the tail, a large nose-tail asymmetry of the distance to the HTS in order to have a lower total proton density but increasing relative PUI density toward the flanks and tail, and a "cooling length" (Schwadron et al. 2014) by PUI charge exchange (see Figures 6–8 in Zirnstein et al. 2016a). These authors also suggested that asymmetric SW flow in the IHS may also affect the extent to which the lobes are observed.

The temporal trends of the lobe centers reflect the global ENA heliotail response to the solar cycle, and provide important information on the recurring dynamics of the heliosphere. As Figure 8(c) shows, the N-lobe and S-lobe move toward the equator as a function of progressing solar activity. This is an effect that is tied to the solar cycle, as demonstrated by Zirnstein et al. (2020). During solar minimum conditions, fast SW propagates through the heliosphere at mid to high latitudes, and thus creates higher-energy ENAs at high latitudes. As slower SW mixes into higher latitudes during solar maximum conditions, more of the slow SW gets into IBEX's lines of sight in these directions, effectively shifting the lobe center toward lower latitudes. This same phenomenon occurs in both lobes and at similar time scales, causing their centers to move eclipticward during solar maximum conditions. The tail lobes thus contain mixed ENAs created by SW from different phases of the solar cycle. As can be seen, the S-lobe is more pronounced and clearer, being located away from possible ribbon contaminations. However, neither of these two lobes' boundaries converges during all time periods to reflect a return and a full cyclic behavior. These results seem to agree well with the physical process proposed by Zirnstein et al. (2020). The authors used this explanation to understand the temporal variations of the derived ENA distance from the HTS.

The C-lobe is offset from the downwind direction by  $13^\circ 24'$  (nonweighted average from five time periods) toward the starboard side, with the closest center value to the downwind being that of 2016–2017. This offset location of the C-lobe has also been reported by Schwadron et al. (2014) and Zirnstein et al. (2016a), and was attributed by these authors to the way the ISMF wraps and squeezes the heliopause. In the current observations, we emphasize that ENAs from the C-lobe are persistently visible around the downwind direction (Figures 1–3) but exhibit an enhancement asymmetry toward the SB-lobe. The source of this asymmetry is unknown but could be an increased contamination or spillover from the closest region of the ribbon, which happens to be brightest at these lower ENA energies ( $< 2$  keV), or an inherent asymmetry in the ENA source region itself.

The P-lobe and SB-lobe depressions exhibit an interesting cyclic effect that is clear in Figure 8(c): as SW conditions move from solar minimum to solar maximum, the P-lobe centers

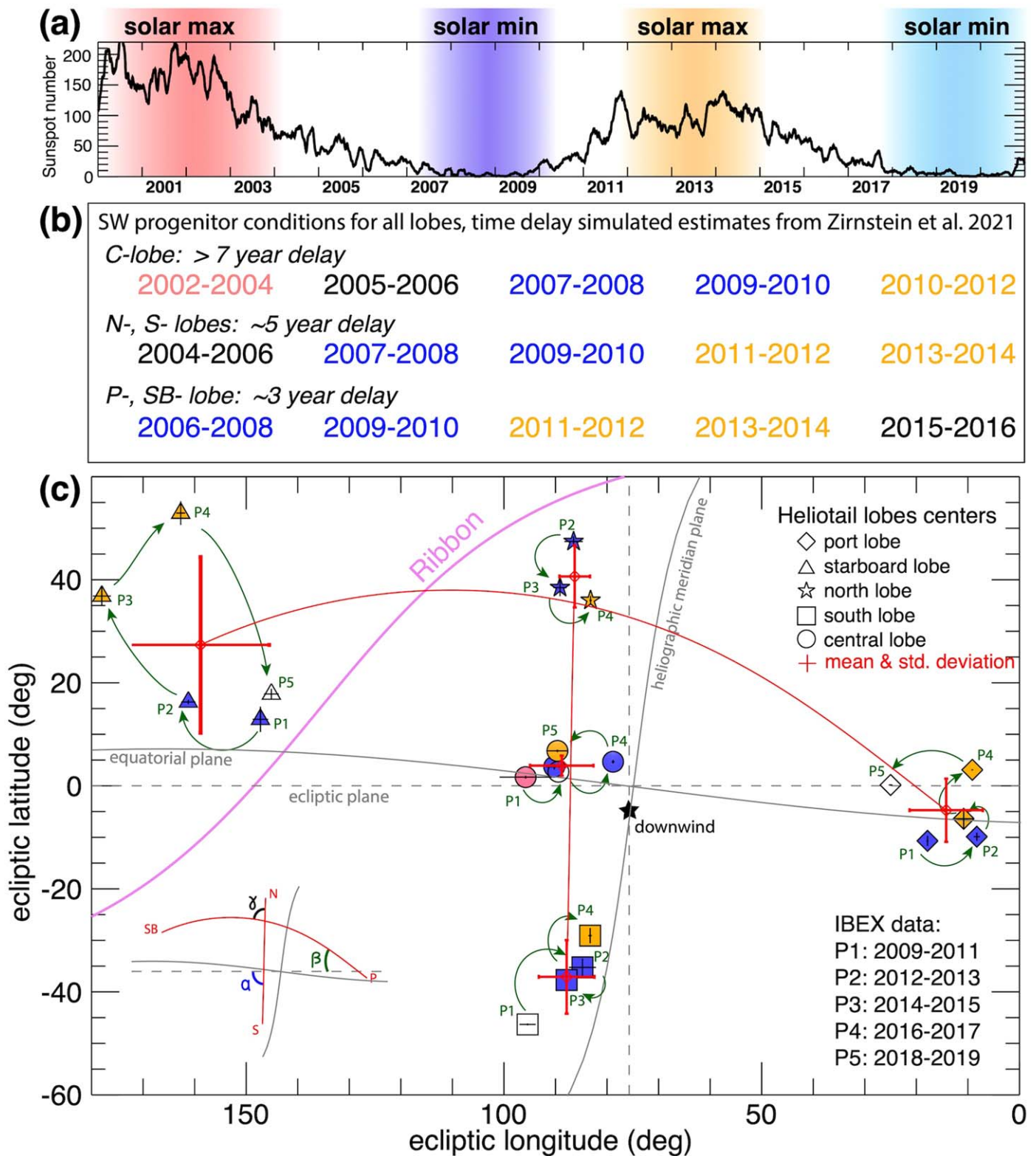


**Figure 8.** A schematic summary of the observations in this study. (a) Sunspot variations indicating the solar cycle phase. (b) SW progenitor conditions mapped to the studied ENA observations, based on estimates from Zirnstein et al. (2020). (c) Summary of the heliotail lobes' motion during a solar cycle. Color coded symbols indicate the centers of the different lobes during different SW conditions. Superposed lines mark the ecliptic, heliographic meridian, and solar equatorial planes (gray), along with the ribbon trace (violet). Green arrows illustrate the motion of the centers with time and red points mark the nonweighted averages of the lobe centers (Table 1). The downwind direction is also marked with a black star.

move in a counterclockwise manner while simultaneously the SB-lobe centers move clockwise, both appearing to be returning to their relative initial positions after ~11 yr. This

effect suggests that regardless of the solar cycle phase, both depression lobes respond in a similar but reflected manner, and are thus reflective of the geometry of the heliosphere. The

**Table 2**

Angles that the Planes Defined by the Ecliptic, North–South, and Port–Starboard Lobe Centers Make at  $\sim 4.3$  keV (see Figure 8(b))

Period	N–S and Ecliptic; $\alpha$ (deg)	SB–P and Ecliptic; $\beta$ (deg)	SB–P and N–S; $\gamma$ (deg)
2009–2011	...	13.31	...
2012–2013	89.04	19.35	76.20
2014–2015	89.18	70.60	75.88
2016–2017	89.94	71.90	71.90
2018–2019	...	20.56	...

P-lobe and SB-lobe are asymmetric with respect to the downwind direction, and the P-lobe averaged center appears to be closer than the SB-lobe; for instance, in years 2011–2012, the P-lobe is  $\sim 76^\circ$  away from the downwind center while the SB-lobe is  $\sim 86^\circ$  away. In 2018–2019, both lobes move away with the P-lobe center at  $\sim 50^\circ$  and the SB-lobe center now at  $\sim 69^\circ$ . Given that the P-lobe and SB-lobe centers move simultaneously in opposite trends and that the SB-lobe center is a bit farther from the downwind direction, this suggests that there may be an asymmetry in the heliosphere with respect to the global plasma flow properties in the IHS and to the IHS thickness.

#### 4.2. Lobes' Relative Locations in the Heliotail

We now move to discuss the tilting in the heliotail lobes and their relative locations with respect to each other and the global configuration of the heliosphere. McComas et al. (2013) first reported that the P-lobe and SB-lobe's tilting can be attributed to the ISMF draping around the heliosphere, squeezing it toward the ISMF direction in the interstellar space. Zirnstein et al. (2016b) exploited this tilt via regression analysis and numerical modeling and suggested a strong relation between this tilt and the asymmetric SW emanating from the Sun. Furthermore, this effect has been observed in simulations by Heerikhuisen et al. (2014) and Zirnstein et al. (2017b), who also attributed it to the ISMF pressure squeezing the heliosphere.

Using the weighted averages of the centers (Table 1) and following the similar terminology of Zirnstein et al. (2016a), we calculate the angles that characterize the relative locations of the lobes in the heliosphere over time, where  $\alpha$  is the angle between the ecliptic plane and the plane containing the N-lobe and S-lobe,  $\beta$  is the angle between the ecliptic plane and the plane containing the P-lobe and the SB-lobe, and  $\gamma$  is the angle between [N-, S-lobe] and [P-, SB-lobe]. These angles are illustrated in the lower left inset of Figure 8(c). Table 2 lists these values. Note that the high-latitude values of the SB-lobe during P3 and P4 drive  $\beta$  to be high during these periods. Nonetheless, it becomes clear that the planes connecting the averaged centers of the lobe pairs are quasi-perpendicular to each other, and that the [N-lobe, S-lobe] plane is quasi-parallel to the heliographic meridian and the [P-lobe, SB-lobe] plane is quasi-parallel to the equatorial plane. The values of these angles obtained from the lobe centers of all periods (nonweighted) are  $\alpha = 89^\circ 03$ ,  $\beta = 38^\circ 02$ , and  $\gamma = 76^\circ 75$ .

The N-lobe and S-lobe are both ENA-enhanced lobes and are located nearly symmetrically from the ecliptic (within a  $6^\circ$  latitude). Both lobes lie on a plane that is slightly tilted ( $\sim 1^\circ$ ) with respect to the ecliptic plane. Albeit small, it is important to

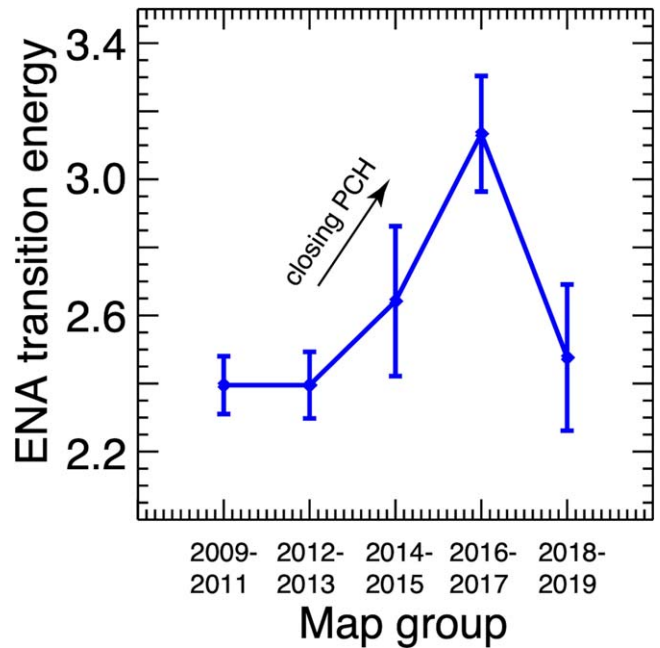


**Figure 9.** Energy at which the tail splits from a C-lobe (most visible at  $\sim 1.1$  keV) into an N-lobe and S-lobe (most visible at  $\sim 4.3$  keV). As shown, the split energy during solar minimum conditions is stable and varies with increasing solar activity, as the slow and fast SW content in the IHS gets modified.

note that this tilt is clockwise (Figure 8(c)) and in the same direction of the P–SB lobes' tilting ( $\sim 38^\circ$ ), suggesting that the ISMF wrapping around the heliosphere is responsible for such a phenomenon. Its effect is thus global and is also apparent at the N- and S-lobe, indicating the rotation of the whole structure of the heliotail by the ISMF. This is well illustrated in Figure 9 of McComas et al. (2013), where the N- and S-lobe are shown tilted in the cartoon, but the tilt was not observed in the early IBEX data then and could not be quantified (see also Zirnstein et al. 2016b, Figure 3). Because of the prevailing cyclic motion of the P-lobe and SB-lobe centers with the solar cycle phase, it becomes clear that for any given period, the line connecting the centers of the lobes oscillates up and down in latitude; that is, the centers on both sides for the same time period go higher or lower in latitude relatively together. The same applies for the N-lobe and S-lobe, as shown. Interestingly, this squeezing phenomenon has also been observed to happen in the Earth's magnetosphere (Sibeck et al. 1985), and most recently, the squeezing and rotation of the magnetotail as a function of the interplanetary magnetic field clock angle has been reported using IBEX magnetospheric observations (e.g., Hart et al. 2021 for IBEX magnetospheric ENA imaging; see also Fuselier et al. 2010; McComas et al. 2011; Dayeh et al. 2015, 2020b; Ogasawara et al. 2019; Starkey et al. 2022).

#### 4.3. Transitioning of the Heliotail

Figure 7 shows that the transitioning of the tail from a C-lobe at  $\sim 1.1$  keV to two north and south lobes at  $\sim 4.3$  keV occurs during all years, but the energy at which the transition occurs changes with time. Note that the transition energy derived here indicates the energy above which we see separate lobes at the IBEX energies. Figure 9 shows how this energy varies with time, revealing that it follows the solar cycle phase, and in particular, the opening and closing of PCHs. During solar

minimum conditions, when the PCHs are open, the transition energy is lower than the value during solar maximum conditions, when the PCHs close. The trend clearly follows this behavior. Zirnstein et al. (2017b) determined that the transition happens because of the different fast-to-slow SW content injected into the IHS. The more of the slow SW that travels to higher latitudes in transition to solar maximum conditions, the lower the plasma temperature that is in the N-lobe and S-lobe—thus, the higher the ENA energy at which the N-lobe and S-lobe would appear (Figure 8; see also Figure 11 in Zirnstein et al. 2017b). For instance, in 2016–2017, the IHS produces fewer high-energy ENAs at mid latitudes due to the closing of PCHs that occurred a few years earlier. Therefore, there are fewer ENAs at high energies coming from the N- and S-lobe of the heliotail. Because  $J_{\text{slow}}$  does not change near the ecliptic plane but  $J_{\text{fast}}$  decreases over time from 2009 to 2017, this implies that  $R_J$  decreases and ENA fluxes between the C-lobe and N/S-lobe become more similar at IBEX energy passbands 4–6 ( $\sim 1.7$ – $4.3$  keV). The effect of this is that IBEX only sees the separate N- and S-lobe at the highest-energy passband centered on  $\sim 4.3$  keV in 2016–2017. Once the PCHs open again, more higher-energy ENAs are produced in the directions of the N/S-lobe, making the N/S-lobe more apparent at energy passband 5 ( $\sim 2.7$  keV).

It is a bit surprising that the tail structures related to the SW do not completely disappear during solar maximum conditions. McComas et al. (2013) speculated that during these conditions, the tail as observed at  $>2$  keV may morph into a single-lobe structure as the slow SW and fast SW mix during solar maximum times; however, this does not appear to happen. There is a clear migration of the N- and S-lobe equatorward, with the transition energy changing from  $\sim 2.4$  to  $\sim 3.2$  keV within a few years. This change suggests that during solar maximum conditions, the slow SW content in the IHS appears to extend drastically to higher latitudes, which is well apparent in the ENA signature, but farther down the heliotail ENAs from the fast/hot SW are still contributing to the line-of-sight integrated flux. These results indicate that the structure of the heliotail is also linked to changes in the SW content in the IHS and that the heliotail has a dynamic profile that should not be ignored when time-independent simulations of the heliosphere are performed.

In summary, results show that the heliotail structure persists over all phases of the solar cycle with unique signatures associated with the different lobes. There is clear evidence that the heliotail lobes evolve with the solar cycle (i.e., with dynamic pressure and PCHs), comprising ENAs originating from SW of different ages and properties. Furthermore, results show that effects of multiple phases of the solar cycle are present in the tail. For example, the evolution of the C-lobe, N-lobe, and S-lobe during 2012–2017 is due to the mixing of fast and slow SW as the solar cycle evolves from minimum to maximum. Finally, the lobes' locations over time exhibit a cyclic motion in the sky, enabling us to predict, for instance, that within 2022–2024, the S- and N-lobe locations would be similar to observations made at the beginning of the IBEX mission (2009–2011).

This work was carried out as part of the IBEX mission, which is part of NASA's Explorer program. Authors M.A.D. and E.J.Z. acknowledge support from NASA grants 80NSSC17K0597 and 80NSSC20K0783. The work at SwRI is partially supported by NASA grant 80NSSC21K0582.

Authors M.A.D. and E.J.Z. acknowledge support from the NASA DRIVE Science Centers initiative, under contract 80NSSC20K0603 in the BU SHIELD DRIVE Science Center.

## ORCID iDs

M. A. Dayeh  <https://orcid.org/0000-0001-9323-1200>  
 E. J. Zirnstein  <https://orcid.org/0000-0001-7240-0618>  
 S. A. Fuselier  <https://orcid.org/0000-0003-4101-7901>  
 H. O. Funsten  <https://orcid.org/0000-0002-6817-1039>  
 D. J. McComas  <https://orcid.org/0000-0001-6160-1158>

## References

- Abbasi, R., Abdou, Y., Abu-Zayyad, T., et al. 2012, *ApJ*, 746, 33  
 Alexashov, D., & Izmodenov, V. 2005, *A&A*, 439, 1171  
 Baliukin, I. I., Izmodenov, V. V., & Alexashov, D. B. 2020, *MNRAS*, 499, 441  
 Baranov, V. B., & Malama, Y. G. 1993, *JGR*, 98, 15157  
 Bzowski, M., Kubiak, M. A., Mbius, E., et al. 2012, *ApJS*, 198, 12  
 Bzowski, M., Swaczyna, P., Kubiak, M. A., et al. 2015, *ApJS*, 220, 28  
 Dayeh, M. A., Farahat, A., Ismail-Aldayeh, H., et al. 2021, *AtmRe*, 261, 105723  
 Dayeh, M. A., Fuselier, S. A., & Funsten, H. O. 2015, *GeoRL*, 42, 2015GL063682  
 Dayeh, M. A., Livadiotis, G., Aminian, F., et al. 2020a, *Int. J. Mol. Sci.*, 21, 2905  
 Dayeh, M. A., McComas, D. J., Allegrini, F., et al. 2012, *ApJ*, 749, 50  
 Dayeh, M. A., Szalay, J. R., Ogasawara, K., et al. 2020b, *GeoRL*, 47, e2020GL088188  
 Dayeh, M. A., Zirnstein, E. J., Desai, M. I., et al. 2019, *ApJ*, 879, 84  
 Fahr, H. J., Kausch, T., & Scherer, H. 2000, *A&A*, 357, 268  
 Funsten, H. O., Allegrini, F., Bochsler, P., et al. 2009a, *SSRv*, 146, 75  
 Funsten, H. O., Allegrini, F., Crew, G. B., et al. 2009b, *Sci*, 326, 964  
 Fuselier, S. A., Allegrini, F., Funsten, H. O., et al. 2009a, *Sci*, 326, 962  
 Fuselier, S. A., Bochsler, P., Chornay, D., et al. 2009b, *SSRv*, 146, 117  
 Fuselier, S. A., Funsten, H. O., Heirtzler, D., et al. 2010, *GeoRL*, 37, L13101  
 Hart, S. T., Dayeh, M. A., Reisenfeld, D. B., et al. 2021, *JGRA*, 126, e2021JA029278  
 Heerikhuisen, J., Pogorelov, N. V., Zank, G. P., et al. 2010, *ApJL*, 708, L126  
 Heerikhuisen, J., Zirnstein, E. J., Funsten, H. O., et al. 2014, *ApJ*, 784, 73  
 Izmodenov, V. V., & Alexashov, D. B. 2015, *ApJS*, 220, 32  
 Izmodenov, V. V., & Alexashov, D. B. 2020, *A&A*, 633, L12  
 Izmodenov, V. V., Malama, Y. G., Ruderman, M. S., et al. 2009, *SSRv*, 146, 329  
 Kombleuth, M., Opher, M., Baliukin, I., et al. 2021, *ApJ*, 921, 164  
 Kombleuth, M., Opher, M., Michael, A. T., et al. 2020, *ApJL*, 895, L26  
 Kubiak, M. A., Swaczyna, P., Bzowski, M., et al. 2016, *ApJS*, 223, 25  
 Livadiotis, G. 2018, *Entrp*, 20, 799  
 McComas, D. J., Alexashov, D., Bzowski, M., et al. 2012a, *Sci*, 336, 1291  
 McComas, D. J., Allegrini, F., Bochsler, P., et al. 2009a, *SSRv*, 146, 11  
 McComas, D. J., Allegrini, F., Bochsler, P., et al. 2009b, *Sci*, 326, 959  
 McComas, D. J., Allegrini, F., Bzowski, M., et al. 2014, *ApJS*, 213, 20  
 McComas, D. J., Buzulukova, N., Connors, M. G., et al. 2012b, *JGRA*, 117, A03225  
 McComas, D. J., Bzowski, M., Dayeh, M. A., et al. 2020, *ApJS*, 248, 26  
 McComas, D. J., Bzowski, M., Fuselier, S. A., et al. 2015, *ApJS*, 220, 22  
 McComas, D. J., Dayeh, M. A., Allegrini, F., et al. 2012c, *ApJS*, 203, 1  
 McComas, D. J., Dayeh, M. A., Funsten, H. O., et al. 2011, *JGRA*, 116, A02211  
 McComas, D. J., Dayeh, M. A., Funsten, H. O., et al. 2013, *ApJ*, 771, 77  
 McComas, D. J., Rankin, J. S., Schwadron, N. A., & Swaczyna, P. 2019, *ApJ*, 884, 145  
 Möbius, E., Bochsler, P., Bzowski, M., et al. 2009, *Sci*, 326, 969  
 Möbius, E., Bochsler, P., Bzowski, M., et al. 2012, *ApJS*, 198, 11  
 Möbius, E., Bzowski, M., Frisch, P. C., et al. 2015, *ApJS*, 220, 24  
 Ogasawara, K., Dayeh, M. A., Fuselier, S. A., et al. 2019, *JGRA*, 124, 8761  
 Opher, M., Bibi, F. A., Toth, G., et al. 2009, *Natur*, 462, 1036  
 Opher, M., Drake, J. F., Zank, G. P., et al. 2021, *ApJ*, 922, 181  
 Opher, M., Drake, J. F., Zieger, B., & Gombosi, T. I. 2015, *ApJL*, 800, L28  
 Parker, E. N. 1961, *ApJ*, 134, 20  
 Pogorelov, N. V. 2016, *JPhCS*, 719, 01203  
 Pogorelov, N. V., Borovikov, S. N., Heerikhuisen, J., & Zhang, M. 2015, *ApJL*, 812, L6

- Pogorelov, N. V., Borovikov, S. N., Zank, G. P., & Ogino, T. 2009, *ApJ*, 696, 1478
- Pogorelov, N. V., Zank, G. P., & Ogino, T. 2006, *ApJ*, 644, 1299
- Schwadron, N. A., Allegrini, F., Bzowski, M., et al. 2011, *ApJ*, 731, 56
- Schwadron, N. A., Bzowski, M., Crew, G. B., et al. 2009a, *Sci*, 326, 966
- Schwadron, N. A., Crew, G., Vanderspek, R., et al. 2009b, *SSRv*, 146, 207
- Schwadron, N. A., Richardson, J. D., Burlaga, L. F., McComas, D. J., & Moebius, E. 2015, *ApJL*, 813, L20
- Schwadron, N. A., & McComas, D. J. 2019, *ApJ*, 887, 247
- Schwadron, N. A., Moebius, E., Fuselier, S. A., et al. 2014, *ApJS*, 215, 13
- Schwadron, N. A., Moebius, E., Kucharek, H., et al. 2013, *ApJ*, 775, 86
- Sibeck, D. G., Siscoe, G. L., Slavin, J. A., et al. 1985, *JGR*, 90, 4011
- Starkey, M. J., Dayeh, M. A., Fuselier, S. A., et al. 2022, *JGRA*, 127, e2021JA030036
- Zank, G. P. 2015, *ARA&A*, 53, 449
- Zhang, M., & Pogorelov, N. 2016, *JPhCS*, 767, 012027
- Zirnstein, E. J., Dayeh, M. A., Heerikhuisen, J., et al. 2021, *ApJS*, 252, 26
- Zirnstein, E. J., Dayeh, M. A., McComas, D. J., & Sokół, J. 2017a, *ApJ*, 846, 63
- Zirnstein, E. J., Dayeh, M. A., McComas, D. J., & Sokół, J. M. 2020, *ApJ*, 897, 138
- Zirnstein, E. J., Funsten, H. O., Heerikhuisen, J., et al. 2016a, *ApJ*, 826, 58
- Zirnstein, E. J., Heerikhuisen, J., Funsten, H. O., et al. 2016b, *ApJL*, 818, L18
- Zirnstein, E. J., Heerikhuisen, J., Zank, G. P., et al. 2014, *ApJ*, 783, 129
- Zirnstein, E. J., Heerikhuisen, J., Zank, G. P., et al. 2017b, *ApJ*, 836, 238